OPTICS

Selectively steering photon spin angular momentum via electron-induced optical spin Hall effect

Cheng Chi†, Qiao Jiang†, Zhixin Liu, Liheng Zheng, Meiling Jiang, Han Zhang, Feng Lin, Bo Shen, Zheyu Fang*

The development of the optical spin Hall effect (OSHE) realizes the splitting of different spin components, contributing to the manipulation of photon spin angular momentum that acts as the information carrier for quantum technology. However, OSHE with optical excitation lacks active control of photon angular momentum at deep subwavelength scale because of the optical diffraction limit. Here, we experimentally demonstrate a selective manipulation of photon spin angular momentum at a deep subwavelength scale via electron-induced OSHE in Au nanoantennas. The inversion of the OSHE radiation pattern is observed by angle-resolved cathodoluminescence polarimetry with the electron impact position shifting within 80 nm in a single antenna unit. By this selective steering of photon spin, we propose an information encoding with robustness, privacy, and high level of integration at a deep subwavelength scale for the future quantum applications.

INTRODUCTION

Quantum information with features of large capacity and high processing speed has been successfully applied in modern signal transmission, processing, memory, etc. (*1*–*3*). The evolution of quantum science to a practical technology promises extreme advantages for specific applications in computation (*4*), simulation (*5*), and cryptography (*6*). In the development of quantum information technology, it is substantial to find a proper information carrier that is required to be highly integrated, and with a large storage capacity to satisfy the need of quantum information applications. Photons have been validated as low-noise information carriers by pioneering works of quantum entanglement, teleportation, and Bell nonlocality (*7*–*10*). As the requirement on information capacity increases, photon spin angular momentum was introduced to provide extra degrees of freedom for carrying quantum information (*11*–*13*).

The optical spin Hall effect (OSHE) provides a unique approach for steering photon spin angular momentum. Photon spin splitting was investigated with the mechanism of spin-orbit interaction (*14*–*18*) and has been applied for planar microcavities (*19*, *20*), metamaterials (*21*–*24*), precision measurements (*25*–*27*), etc. By considering that the photon spin angular momentum acts as an information carrier with high robustness and large capacity, OSHE is predicted to have potential in manipulating the information carrier for quantum technology, especially in information encoding and cryptography with features of orthogonality and high dimensionality. Previous studies on steering OSHE mainly focuses on the structure design (*28*–*30*), where the photon spin manipulation can be realized with Pancharatnam-Berry and Rytov-Vladimirskii-Berry phase shift (*31*–*33*), which were used to explain the underlying physics of the OSHE with spin-orbit interaction of light. A recent study proposed an electrical tuning method of OSHE in a liquid crystal microcavity (*34*). However, this approach is difficult to integrate at the nanoscale. An efficient solution in selectively steering OSHE needs to be proposed to realize its potential in the quantum information technology and device applications (*35*), where the obstacle of the light diffraction limit should be solved for future device integration.

As one of the noninvasive high-resolution detection methods (*36*–*40*), cathodoluminescence (CL) polarimetry with precise control of the electron impact position overcomes the light diffraction limit (*41*) and has been successfully used for electromagnetic field investigation at deep subwavelength scale (*42*, *43*). Under the electron beam stimulation, deep subwavelength shift of excitation position can directly regulate the distribution of local density of states (LDOS) (*44*–*46*), contributing to the evolution of far-field CL emission. Angle-resolved CL polarimetry as a characterization of photon momentum space can effectively detect the radiation direction. Hence, angle-resolved CL imaging polarimetry can explore photon spin with far-field angular patterns and allows investigating polarization-dependent phenomena with high spatial and angular resolution. This characterization technique overcomes the light diffraction limit; thus, it can be used to observe the electron-induced OSHE at deep subwavelength scale, which paves the way for the selective steering of photon spin under electron excitation.

In this work, we demonstrate the selective manipulation of photon spin angular momentum via electron-induced OSHE on a plasmonic nanoantenna with precisely engineered multipole moments. With an electron beam excitation position shift at deep subwavelength scale, splitting of left-handed circularly polarized (LCP) and right-handed circularly polarized (RCP) photon spin components can be observed by angle-resolved CL imaging polarimetry with the electron beam impact position located at the edge of Au nanoantenna. The radiation pattern of LCP and RCP can be inverted by changing the electron beam impact position, while the nonsplitting pattern of spin states can be detected with the electron impinging position located at the center of the Au nanoantenna. The switch of photon spin splitting between "turn-on" and "turn-off" states can be effectively achieved by altering the interference of dipole and quadrupole moments, leading to a selective manipulation of photon spin. Based on this electron-induced OSHE, we realize a spin-dependent binary encoding within a single Au nanoantenna. This capability of OSHE excitation with electron beam provides a compelling platform for

School of Physics, State Key Lab for Mesoscopic Physics, Academy for Advanced Interdisciplinary Studies, Collaborative Innovation Center of Quantum Matter, and Nano-optoelectronics Frontier Center of Ministry of Education, Peking University Yangtze Delta Institute of Optoelectronics, Peking University, Beijing 100871, China.
*Corresponding author. Email: zhyfang@pku.edu.cn
†These authors contributed equally to this work.

the manipulation of photon spin and paves the way for the future quantum information processing and devices design.

RESULTS

The electron-induced OSHE refers to the phenomenon of photon spin splitting, where asymmetrical radiation pattern is observed with separation of spin components under electron excitation (Fig. 1A). The single Au nanoantenna was fabricated at the size of 200 × 80 nm using electron beam lithography with the deposition of 30-nm Au and 2-nm Ti as an adhesive layer. To investigate the far-field behavior of different spin components, the photon spin splitting schematic (Fig. 1B) is introduced to analyze Stokes parameters as S_1, S_2, and S_3 on [θ, ϕ] space in vector spherical harmonics (note S1), which is the general representation of polarization and can be used to retrieve polarization-related quantity (*47*). All CL measurements are performed in a scanning electron microscope (SEM; FEI Quattro C) equipped with a specialized CL detection system (Delmic), which consists of a parabolic mirror, rotating-plate polarimetry optics, and a highly sensitive complementary metal-oxide semiconductor (CMOS) array as shown in Fig. 1C. The electron beam passing through the pinhole of the parabolic mirror can effectively excite the sample, and the CL emission can be collected by the mirror and is measured using the CMOS array. A quarter-wave plate together with a linear polarizer is placed in the light path for extracting different spin components of the CL emission. Far-field angular patterns of different spin components can be acquired at target wavelength by the angle-resolved CL imaging polarimetry.

When the center of the upper edge was excited, the CL emission of the Au nanoantenna was analyzed both in spectra and far-field angular patterns. Circularly polarized (CP)–resolved CL spectra (Fig. 2A) show that LCP and RCP components exhibit comparable CL intensities with their emission peaks both located at the wavelength around 630 nm, agreeing well with the simulation result (fig. S1), with slight red-shift compared with the LSP resonance (fig. S2). To characterize the difference of polarization states, the CL chirality is defined as $|I_{RCP} - I_{LCP}|/(I_{RCP} + I_{LCP})$, where I_{LCP} (I_{RCP}) is the CL intensity of LCP (RCP) emission. Around the peak wavelength of 630 nm, LCP and RCP CL intensities are nearly equivalent with the CL chirality smaller than 5%, which is in accordance with the experiment results of chiral LDOS distribution (fig. S3).

Far-field patterns of different spin components were acquired with angle-resolved CL imaging polarimetry. The angular pattern as shown in Fig. 2D reflects the omnidirectionality feature of the CL emission from the symmetrical metallic nanoantenna. However, analyses on different spin components of the CL emission reveal asymmetrical features. Although the observed symmetrical distribution of I_H and I_V (constructed from cartesian fields of I_θ and I_ϕ; Fig. 2B) indicates nondirectional pattern of horizontal and vertical states, the far-field angular patterns of I_{LCP} and I_{RCP} both show obvious directionality, which locate at left and right halves of the hemisphere, respectively (Fig. 2C). To explore the far-field behavior of the LCP and RCP components, the angular pattern of the S_3 Stokes parameter was investigated, where direction splitting of the LCP and RCP components was observed (Fig. 2E), agreeing well with the simulation result (fig. S4). This result demonstrates the far-field

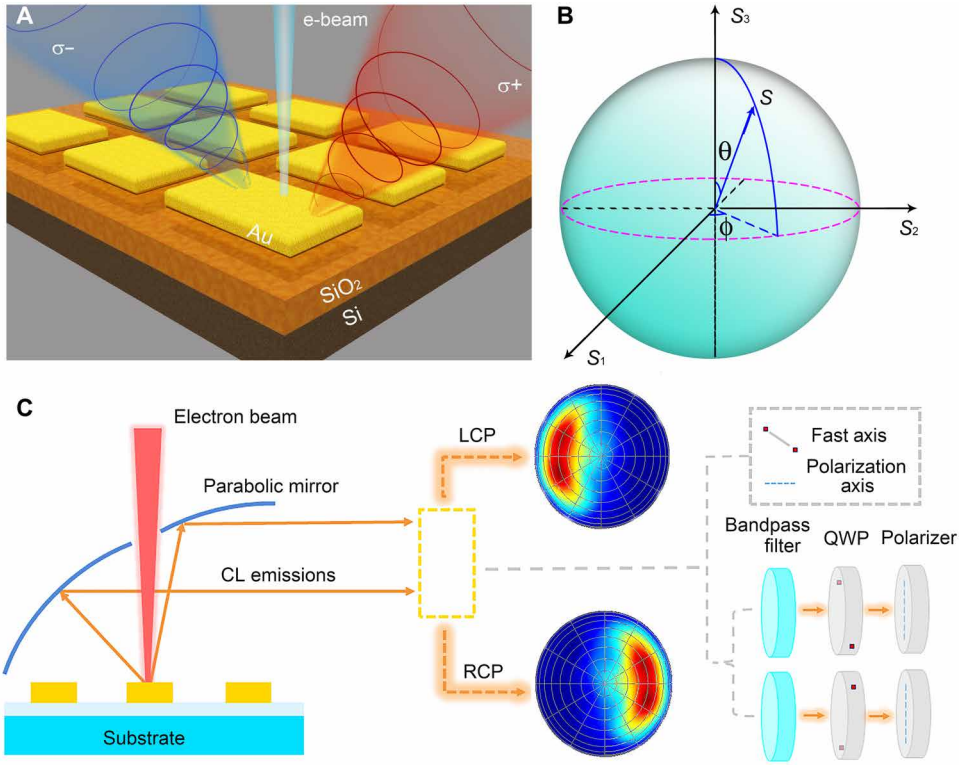

Fig. 1. Schematic of spin component detection. (**A**) Schematic illustration of electron-induced OSHE. Symmetrical Au nanorectangle antenna under electron beam excitation at the upper edge generates asymmetrical circularly polarized radiation. (**B**) Schematic illustration of photon spin analyzing. (**C**) Angle-resolved CL polarimetry for measurements of the circularly polarized radiation. The quarter wave plate and linear polarizer are used to extract circularly polarized components of CL emission.

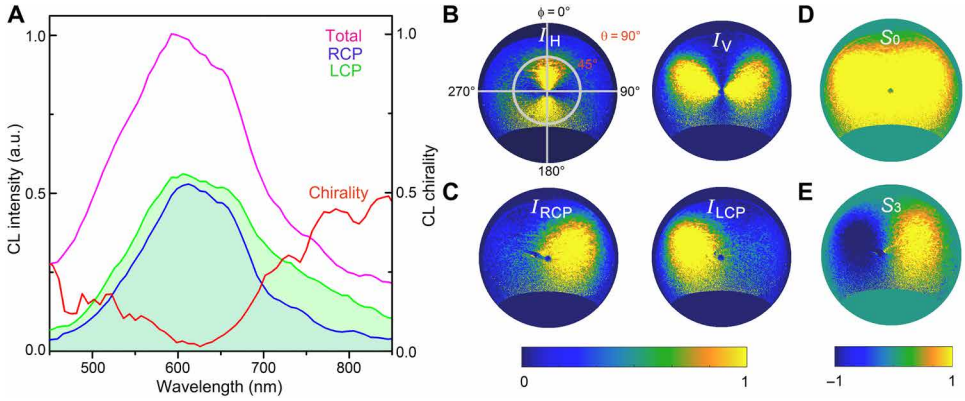

Fig. 2. Analyses of spin states. (**A**) Experimental total, LCP, and RCP CL spectra obtained from Au nanoantenna with the size of 200 × 80 nm under 30-keV electron beam excitation. The stimulation position is located at middle of the upper edge of the Au nanoantenna, with the measured CL chirality corresponding to the right ordinate. (**B**) Measured angular patterns of horizontal (I_H on the left) and vertical (I_V on the right) components for CL signals. The stimulation position is located at the middle of the upper edge of the Au nanoantenna, with the detection wavelength at 650 nm. (**C**) Measured angular patterns of RCP (left) and LCP (right) components for CL signals. The stimulation position and detection wavelength are the same as in (B). (**D**) Measured angular pattern of S_0 Stokes parameter. (**E**) Measured angular pattern of S_3 Stokes parameter. All patterns are normalized to 1. Axis in (C) to (E) is the same as in (B).

pattern difference between LCP and RCP spin components, which can be applied for the manipulation of photon spin, while probing the same sample with a diffraction-limit optical spot will wash out the observed OSHE (fig. S5). By further analyzing the calculated near-field signal of the LCP and RCP components, distinct spatial separation of their near-field patterns was observed, which resulted in the splitting of LCP and RCP components in the far field. This splitting feature together with the equivalence of LCP and RCP intensities indicates the existence of electron-induced OSHE.

Selective manipulation of spin angular momentum at deep subwavelength scale by electron-induced OSHE is shown in Fig. 3. Three excitation positions were chosen to illustrate this manipulation at detected wavelengths of 600 and 650 nm, respectively (Fig. 3A). For the impinging position at the middle of the upper edge, the far-field S_3 angular pattern shows photon spin splitting with LCP and RCP components located at the left and right halves of the angular hemisphere, which demonstrates a turn-on state of OSHE. For the excitation position located at the center of the nanoantenna, the splitting between LCP and RCP components is not observed, which shows regression to the turn-off state of OSHE. For the excitation position located at the middle of lower edge, the relative location of LCP and RCP components inverts in the splitting pattern, which shows returning to the turn-on state. The switch from the turn-on to the turn-off state can be achieved with the electron beam shift within 40 nm, and the inversion of the angular pattern can also be realized with excitation position shift within 80 nm, demonstrating an efficiently selective manipulation of photon spin by electron-induced OSHE. As shown in Fig. 3B, simulation results reveal the angular pattern evolution with electron beam moving over three chosen positions, which is consistent with the experiment results. For detected wavelengths of 550 and 700 nm with more deviation from the peak wavelength (λ_0), experiment and simulation results (fig. S6) both show OSHE patterns with lower S_3 intensity. These results indicate that in the far-field angular pattern, the S_3 intensity increases as detected wavelength λ increases, and decreases after $\lambda = \lambda_0$. This observation reveals that the suitable λ for detecting OSHE under electron excitation is around 630 nm for the studied Au nanoantenna.

To explore the directionality of spin states under different excitation positions, the scattering ratio of LCP was acquired as the function of wavelength, which is defined as the intensity ratio of the half angular hemisphere with lower intensity to the whole angular hemisphere. The experimental data show that the measured scattering ratio remains beyond 20% when excited at the upper or lower edge (Fig. 3C), which indicates the emission directionality of the LCP state in far-field angular pattern. To investigate the splitting feature of LCP and RCP components, S_3 values integrated on the left and right halves of the angular hemisphere were acquired with error bar to describe the uncertainty of experiments (Fig. 3D). To quantitatively describe the splitting difference in angular S_3 patterns, S_3 ratio (ρ) is defined as $|S_{3left}|/S_{3right}$, where S_{3left} (S_{3right}) is the integrated S_3 value of the left (right) half of the angular hemisphere. Experiment results show that when the electron excitation position is located at the upper edge, ρ remains around 1 at the detected wavelength range from 550 to 700 nm, with deviation below 15%. With the stimulation position located at the lower edge, ρ remains around −1 at same detected wavelength range with deviation below 12%. These analyses reflect the splitting pattern difference of LCP and RCP components under different impinging positions, which verifies the steering of electron-induced OSHE with stimulation position shift at deep subwavelength scale, thus realizing the selective manipulation of the spin angular momentum.

To explore the mechanism of electron beam–induced OSHE, far-field angular patterns of different-sized Au nanoantennas were investigated with angle-resolved CL polarimetry. The angular patterns of the S_3 Stokes parameter are shown in Fig. 4A, where distinguishable LCP and RCP component splitting with an equivalent intensity (fig. S7) validates the existence of OSHE in different nanoantennas. Experimental results show that at the detected wavelength of 650 nm, the S_3 intensity increases as the size of the Au nanoantennas increases, agreeing well with simulation results (Fig. 4B).

To elucidate the underlying physics of observed OSHE under electron stimulation, scattering intensity of different multipole moments was investigated with the multipolar decomposition, where the calculated scattered field was decomposed into vector spherical

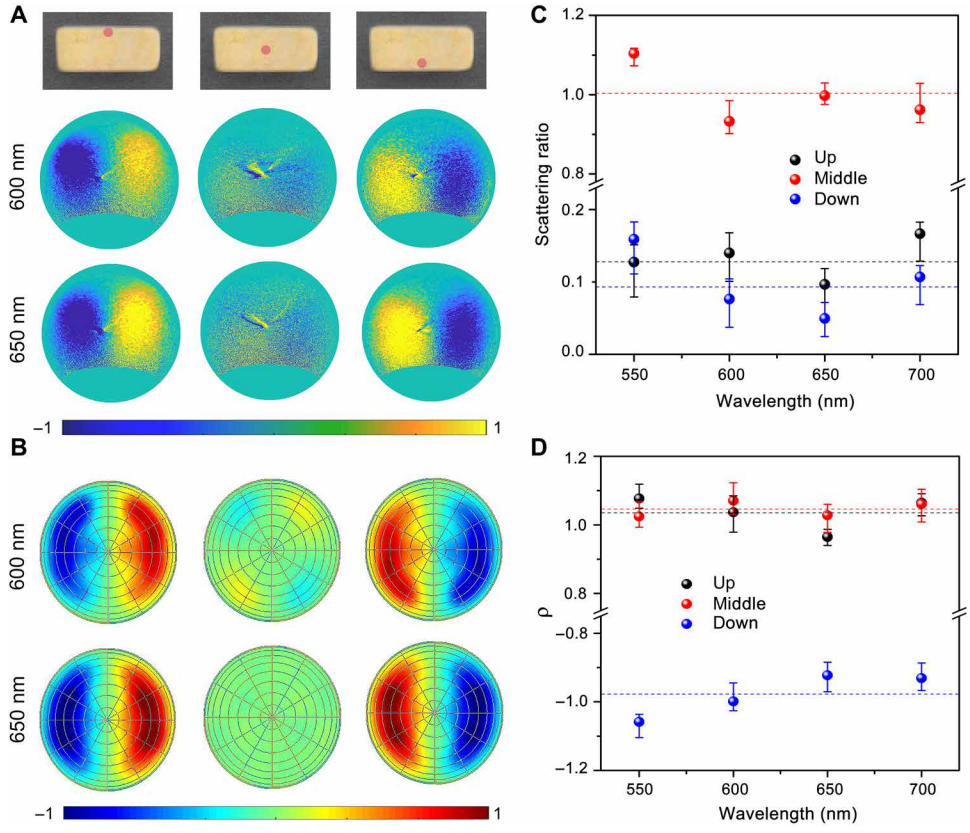

Fig. 3. Manipulation of photon spin angular momentum. (**A**) Experimental normalized angular CL S_3 patterns obtained from Au nanoantenna at the size of 200 × 80 nm, with electron stimulation voltage of 30 keV. Stimulation positions located at the middle of the upper edge, center of the antenna, and middle of the lower edge, which are marked with a red point on the pseudocolor scanning electron microscopy (SEM) image of the Au nanoantenna. Collected wavelengths are 600 and 650 nm, respectively. (**B**) Simulated angular CL S_3 patterns of the Au nanoantenna. Electron beam excitation positions and collected wavelengths are the same as in (A). (**C**) Scattering ratio as function of wavelength for different excitation positions. The horizontal dashed line corresponds to the averaged scattering ratio. Error bar represents the uncertainty of scattering ratio in three experiments. (**D**) S_3 ratio (ρ) as a function of wavelength for different excitation positions. S_3 ratio (ρ) is defined as $|S_{3left}|/S_{3right}$, where S_{3left} (S_{3right}) is the integrated S_3 value of the left (right) half of the angular hemisphere. The horizontal dashed line corresponds to the averaged ρ. Error bar represents the uncertainty of ρ in three experiments.

harmonics according to the general multipole scattering theory (*48*–*50*)

$$I = \frac{2\omega^4}{3c^3}|P|^2 + \frac{2\omega^4}{3c^5}|M|^2 + \frac{4\omega^5}{3c^5}(P\bullet T) + \frac{2\omega^6}{3c^7}|T|^2 + \frac{\omega^6}{5c^5}\sum|Q_{\alpha\beta}|^2 + \frac{\omega^6}{40c^7}\sum|M_{\alpha\beta}|^2 + O\left(\frac{1}{5c^7}\right) \quad (1)$$

where P, M, T, $Q_{\alpha\beta}$, and $M_{\alpha\beta}$ correspond to the electrical dipole, magnetic dipole, toroidal dipole, electrical quadrupole, and magnetic quadrupole; c is the speed of light in vacuum; α, β = x, y, z. Relevant components for edge excitation are P_y, P_z, M_y, and $Q_{\alpha\alpha}$, which are calculated with asymptotic far-field approximations for dipoles and quadrupoles in the presence of a substrate. P_y and P_z components are featured by characteristic toroid shapes with significant E_z component at the edge of the nanoantenna, which are suitable for electron beam steering. M_y component results in the electrical current loop on the xz plane. $Q_{\alpha\alpha}$ quadrupoles show multipole radiation lobes in the far-field pattern. From the finite-difference time-domain (FDTD) simulation data, scattering intensity of these multipole moments (Fig. 4C) is calculated, which reflects the contribution of P and Q moments in the far-field angular pattern. This result indicates that at the wavelength range from 550 to 700 nm, the interference of the P and Q moments leverages the far-field angular pattern, where the λ-related feature of interference mode results in the angular pattern evolution with the wavelength increasing as shown in Fig. 3A. Further calculations of the scattering intensity of electrical dipole moments reveal that P_y is the major component in the far-field radiation of the electric dipole (Fig. 4D), where the stimulation position on the symmetry axis inhibits the excitation of P_x. The calculation of the scattering intensity of electrical quadrupole moments shows that Q_{xx}, Q_{yy}, and Q_{zz} are three major components in the far-field radiation of the quadrupole (fig. S8). With the excitation position located at the middle of the upper edge of the Au nanoantenna, the contribution of the P and Q modes is dominant in the far-field angular pattern, where the phase difference of π/2 between the quadrupole and dipole moments results in this spin splitting between the LCP and RCP components (notes S2 and S3). The size difference of Au nanoantennas results in the shift of multipole moment proportions, where the proportion difference between the P and Q moments increases as the size of nanoantenna increases and results in the far-field splitting pattern evolution of LCP and RCP states.

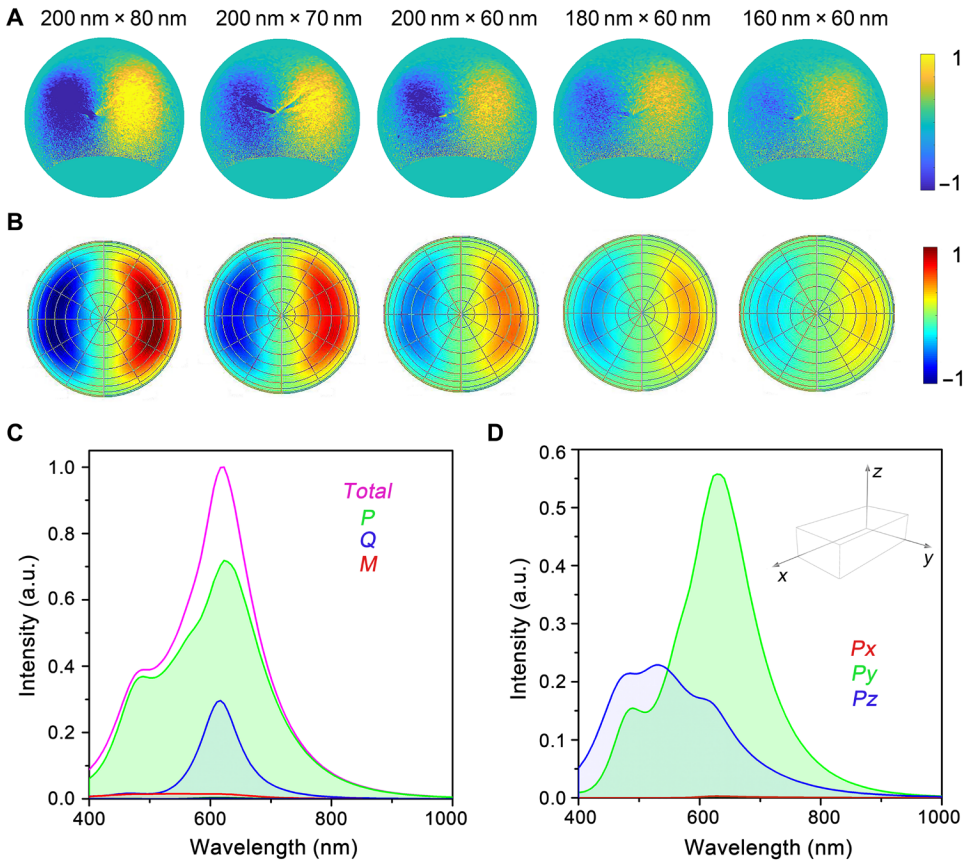

Fig. 4. Multipolar analysis of CP-resolved angular patterns for Au nanoantenna. (**A**) Experimental normalized angular S_3 patterns obtained from Au nanoantennas at the size of 200 × 80, 200 × 70, 200 × 60, 180 × 60, and 160 × 60 nm. The stimulation position is located at the middle of the upper edge of the Au nanoantenna, with 30-keV electron beam excitation. The collected wavelength is 650 nm. (**B**) Simulated angular S_3 patterns of Au nanoantenna at different sizes. The Au nanoantenna size, excitation position, and collected wavelength are the same as in (A). (**C**) Simulated scattering intensity of various multipole moments in nanoantenna with the size of 200 × 80 nm. Spectra correspond to total intensity and intensity of *P*, *Q*, and *M* moments. (**D**) Simulated scattering intensity of various electrical dipole components in the nanoantenna with the size of 200 × 80 nm. Spectra correspond to the intensity of P_x, P_y, and P_z components. Inset: axis (*xyz*) of the dipole orientation.

The steering of OSHE under electron excitation with nanoscale impinging position movement can be applied for a spin-dependent binary encoding, where the manipulation of photon spin mediated by beam shift at deep subwavelength scale carries information, thus is an advantage in module integration. The coding mode is dependent on S_3 Stokes parameter of the radiation, where two different LCP and RCP splitting patterns on the left and right halves of the angular hemisphere are defined as 0 and 1. Erasure code defined from the nonsplitting pattern is introduced to improve the information accuracy. These three modes of 0, 1, and erasure code correspond to the electron beam excitation positions on the upper edge, lower edge, and center of the encoding unit (Fig. 5A). The whole encoding process was integrated to a single unit at the deep subwavelength scale.

In this spin-dependent binary encoding, the encoding unit was designed and fabricated with the size of 200 × 80 nm, where scanning paths were designed according to ASCII (American Standard Code for Information Interchange) codes (Fig. 5B). With electron beam moving along these two paths, capital letters "P" and "K" were encoded and far-field detected (Fig. 5C). This binary encoding introduces photon spin rather than beam intensity as the carrier to promote information processing ability, which increases information capacity on the basis of intensity measurement. The chiral LDOS distribution difference between the LCP and RCP components (fig. S3) presents the polarization-related information with different free-electron impact position. The equivalence of LCP and RCP intensity prevents the information from being read out by intensity detection, where the dissimilarity in angular patterns of photon spin splitting is the key to declassify the signal. Moreover, the introduction of erasure code improves the robustness in the encoding process, contributing to a reliable encoding solution. This spin-dependent binary encoding overcomes the light diffraction limit by applying electron excitation and realizes the deep subwavelength scale leverage of photon spin angular momentum that acts as the coding information, thus benefitting the integration of future quantum devices.

Besides, the photon spin can be used for the classical binary encoding of information; for future work, the single-qubit quantum state tomography can be further used to test whether the spin degree of freedom of emitted light is an actual qubit or a mixed state, which opens a route for studying free-electron quantum optics and broadening quantum technology applications. On the other side, recent advances in ultrafast electron microscopy also can be applied for an ultrafast spin-orbit-coupling modulation by using free electrons. If the free-electron wave packet is modulated with the femtosecond

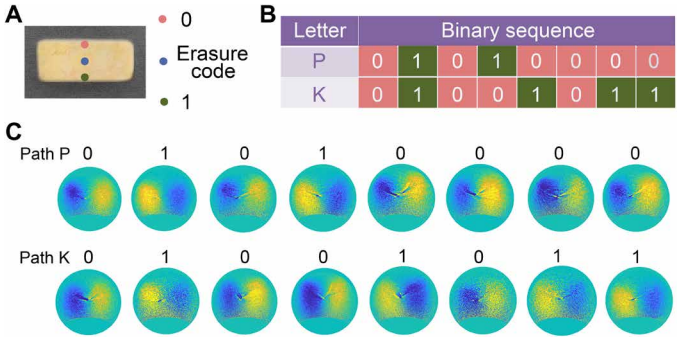

Fig. 5. Schematic of spin-dependent binary encoding. (**A**) Functional unit for spin-dependent binary encoding. With electron beam excitation positions located at the middle of the upper edge, middle of the lower edge, and center of the nanoantenna, which are marked with three points on the pseudocolor SEM image of the Au nanoantenna; corresponding S_3 patterns are defined as 0, 1, and erasure code for binary encoding. (**B**) ASCII codes of capital letters "P" and "K" for the binary encoding. (**C**) Angular CL S_3 patterns with the electron beam moving along two paths corresponding to ASCII codes, which output the binary sequences of "01010000" and "01001011" corresponding to capital letters "P" and "K," respectively.

time resolution, then this modulation speed can be transmitted to the photon polarization modulation, which has potential in the contribution to realizing high-speed quantum information transfer.

DISCUSSION

In summary, we have demonstrated a unique approach for selectively steering photon spin angular momentum at deep subwavelength scale via electron-induced OSHE. The switch between the "on" and "off" states of OSHE was realized with electron beam shift within 40 nm, and the far-field radiation pattern inversion was observed with the impact position moving within 80 nm, where multipole moments excited by electrons leveraged the pattern evolution of photon spin splitting. Furthermore, as spin angular momentum can act as an excellent information carrier for quantum information applications, we demonstrate a spin-dependent binary encoding within a single unit. Features of deep subwavelength scale steering, large information capacity, and high privacy make it a promising candidate for quantum information storage and processing, where high integration and robustness raise this design practicability in devices. Our work provides a demonstration and experimental configuration of steering photon spin via electron-induced OSHE, which can inspire research on modern interdisciplines in spin-orbit interaction, chiral quantum optics, and related applications in quantum information technology in combination with single emitters.

MATERIALS AND METHODS

Some of following methods are similar to those previously published in (*44*).

Sample fabrication

Au nanostructures were fabricated on a Si/SiO_2 substrate with a standard EBL (electron beam lithography) process followed by a lift-off process and Ar ion irradiation. A positive resist {MircoChem PMMA [poly(methyl methacrylate)], A2 950} was spin coated onto the substrate with the thickness of ~60 nm. Structures were patterned by using a focused 30-keV electron beam controlled by the Nano Pattern Generation System module, which is equipped on the SEM (FEI Quanta 450 FEG). A 30-nm Au layer was deposited on the substrate by using an electron beam evaporator (LJUHV E-400 L). Ar ion irradiation was performed for 1 min to clean up the residual PMMA in the final process.

CL measurements

CL angular patterns were acquired by a CL detector system (Delmic SPARC), which is mounted on the SEM (Thermo Fisher Scientific Quattro C). The emission was collected by a highly sensitive CMOS to characterize the far-field angular pattern. Angular collection range is up to 1.49π sr, with angular resolution <10 mrad. For detecting specific wavelengths of the CL emission, different bandpass filters were placed in the optical path. For CP-resolved CL detection, quarter-wave plate and linear polarizer combinations were used in the polarization analyzer module for different detection wavelength ranges. Specifically, the LCP and RCP CL emissions can be selectively collected by orienting the fast axis of the wave plate by ±45° with respect to the polarization axis of the polarizer.

Numerical simulations

All simulation results in this report were all accomplished by commercial FDTD methods solver (FDTD Solutions, Lumerical). The simulation domain included the structure with perfectly matched layers in all directions. For the calculation of scattering, total-field scattered-field sources with linear and circular polarization were used to illuminate the structure along the $-z$ axis. In the calculation of CL emissions, the electron beam moving along the $-z$ axis was regarded as a linear current density $\mathbf{J}(\mathbf{r}, t) = \rho v \delta(z + vt)\ \delta(x - x_0)\ \delta(y - y_0)\ \boldsymbol{n}_z$, where ρ is the electron charge, v is the velocity of electron, $\mathbf{r} = (x_0, y_0, z)$ is the position of electron beam, and $\boldsymbol{n}_z$ is the unit vector along the $+z$ direction. In the frequency domain, it corresponds to a current density as $\mathbf{J}(\mathbf{r}, \omega) = \rho e^{-i\omega z/v} \delta(x - x_0)\ \delta(y - y_0)\ \boldsymbol{n}_z$, the current density was modeled as a series of dipoles with a temporal phase delay ($-z/v$) related to the electron velocity, $v = 0.34c$, corresponding to 30-keV electron energy (c is the velocity of light in a vacuum). A reference simulation (without the nanostructure and substrate) was also run to subtract any background signal created by the electron beam that could obscure the signal from the nanostructure. CL spectra were calculated in the far field by integrating the Poynting vector normal to an arbitrary surface in the upper z half-plane for wavelengths ranging from 400 to 1000 nm. In the far-field region, the time-averaged magnitude of the Poynting vector in spherical coordinates can be expressed as $P_{\text{total}} = \varepsilon_0 c(|\mathbf{E}_\theta|^2 + |\mathbf{E}_\varphi|^2)/2$, $P_{\text{LCP}} = \varepsilon_0 c(|\mathbf{E}_\theta - i\mathbf{E}_\varphi|^2)/4$, and $P_{\text{RCP}} = \varepsilon_0 c(|\mathbf{E}_\theta + i\mathbf{E}_\varphi|^2)/4$ for the total, LCP, and RCP CL spectra calculation. The far-field region was set as a vacuum. In simulations, Palik data for the Au (gold), Si (silicon) complex refractive indices were used. The refractive index of SiO_2 was taken as 1.5.

SUPPLEMENTARY MATERIALS

Supplementary material for this article is available at http://advances.sciencemag.org/cgi/content/full/7/18/eabf8011/DC1

REFERENCES AND NOTES

1. N. Gisin, R. Thew, Quantum communication. *Nat. Photonics* **1**, 165–171 (2007).
2. A. I. Lvovsky, B. C. Sanders, W. Tittel, Optical quantum memory. *Nat. Photonics* **3**, 706–714 (2009).

3. J. Wang, F. Sciarrino, A. Laing, M. G. Thompson, Integrated photonic quantum technologies. *Nat. Photonics* **14**, 273–284 (2019).
4. T. D. Ladd, F. Jelezko, R. Laflamme, Y. Nakamura, C. Monroe, J. L. O'Brien, Quantum computers. *Nature* **464**, 45–53 (2010).
5. A. Aspuru-Guzik, P. Walther, Photonic quantum simulators. *Nat. Phys.* **8**, 285–291 (2012).
6. N. Gisin, G. Ribordy, W. Tittel, H. Zbinden, Quantum cryptography. *Rev. Mod. Phys.* **74**, 145–195 (2002).
7. L. K. Shalm, E. Meyer-Scott, B. G. Christensen, P. Bierhorst, M. A. Wayne, M. J. Stevens, T. Gerrits, S. Glancy, D. R. Hamel, M. S. Allman, K. J. Coakley, S. D. Dyer, C. Hodge, A. E. Lita, V. B. Verma, C. Lambrocco, E. Tortorici, A. L. Migdall, Y. Zhang, D. R. Kumor, W. H. Farr, F. Marsili, M. D. Shaw, J. A. Stern, C. Abellán, W. Amaya, V. Pruneri, T. Jennewein, M. W. Mitchell, P. G. Kwiat, J. C. Bienfang, R. P. Mirin, E. Knill, S. W. Nam, Strong loophole-free test of local realism. *Phys. Rev. Lett.* **115**, 250402 (2015).
8. J. M. Raimond, M. Brune, S. Haroche, Manipulating quantum entanglement with atoms and photons in a cavity. *Rev. Mod. Phys.* **73**, 565–582 (2001).
9. M. Riebe, H. Häffner, C. F. Roos, W. Hänsel, J. Benhelm, G. P. T. Lancaster, T. W. Körber, C. Becher, F. Schmidt-Kaler, D. F. V. James, R. Blatt, Deterministic quantum teleportation with atoms. *Nature* **429**, 734–737 (2004).
10. X.-L. Wang, X.-D. Cai, Z.-E. Su, M.-C. Chen, D. Wu, L. Li, N.-L. Liu, C.-Y. Lu, J.-W. Pan, Quantum teleportation of multiple degrees of freedom of a single photon. *Nature* **518**, 516–519 (2015).
11. X. Liu, M. C. Hersam, 2D materials for quantum information science. *Nat. Rev. Mater.* **4**, 669–684 (2019).
12. E. Nagali, F. Sciarrino, F. De Martini, L. Marrucci, B. Piccirillo, E. Karimi, E. Santamato, Quantum information transfer from spin to orbital angular momentum of photons. *Phys. Rev. Lett.* **103**, 013601 (2009).
13. T. Stav, A. Faerman, E. Maguid, D. Oren, V. Kleiner, E. Hasman, M. Segev, Quantum entanglement of the spin and orbital angular momentum of photons using metamaterials. *Science* **361**, 1101–1104 (2018).
14. S. Fu, C. Guo, G. Liu, Y. Li, H. Yin, Z. Li, Z. Chen, Spin-orbit optical Hall effect. *Phys. Rev. Lett.* **123**, 243904 (2019).
15. K. Y. Bliokh, F. J. Rodríguez-Fortuño, F. Nori, A. V. Zayats, Spin–orbit interactions of light. *Nat. Photonics* **9**, 796–808 (2015).
16. K. Y. Bliokh, C. T. Samlan, C. Prajapati, G. Puentes, N. K. Viswanathan, F. Nori, Spin-Hall effect and circular birefringence of a uniaxial crystal plate. *Optica* **3**, 1039–1047 (2016).
17. B. D. Clark, C. J. De Santis, G. Wu, D. Renard, M. J. McClain, L. Bursi, A.-L. Tsai, P. Nordlander, N. J. Halas, Ligand-dependent colloidal stability controls the growth of aluminum nanocrystals. *J. Am. Chem. Soc.* **141**, 1716–1724 (2019).
18. Z. Shao, J. Zhu, Y. Chen, Y. Zhang, S. Yu, Spin-orbit interaction of light induced by transverse spin angular momentum engineering. *Nat. Commun.* **9**, 926 (2018).
19. A. Kavokin, G. Malpuech, M. Glazov, Optical spin Hall effect. *Phys. Rev. Lett.* **95**, 136601 (2005).
20. C. Leyder, M. Romanelli, J. P. Karr, E. Giacobino, T. C. H. Liew, M. M. Glazov, A. V. Kavokin, G. Malpuech, A. Bramati, Observation of the optical spin Hall effect. *Nat. Phys.* **3**, 628–631 (2007).
21. M. Kim, D. Lee, T. H. Kim, Y. Yang, H. J. Park, J. Rho, Observation of enhanced optical spin Hall effect in a vertical hyperbolic metamaterial. *ACS Photonics* **6**, 2530–2536 (2019).
22. P. V. Kapitanova, P. Ginzburg, F. J. Rodríguez-Fortuño, D. S. Filonov, P. M. Voroshilov, P. A. Belov, A. N. Poddubny, Y. S. Kivshar, G. A. Wurtz, A. V. Zayats, Photonic spin Hall effect in hyperbolic metamaterials for polarization-controlled routing of subwavelength modes. *Nat. Commun.* **5**, 3226 (2014).
23. X. Ling, X. Zhou, X. Yi, W. Shu, Y. Liu, S. Chen, H. Luo, S. Wen, D. Fan, Giant photonic spin Hall effect in momentum space in a structured metamaterial with spatially varying birefringence. *Light Sci. Appl.* **4**, e290 (2015).
24. N. Shitrit, I. Yulevich, E. Maguid, D. Ozeri, D. Veksler, V. Kleiner, E. Hasman, Spin-optical metamaterial route to spin-controlled photonics. *Science* **340**, 724–726 (2013).
25. F. Wang, Z. Sun, C. Xu, L. Yang, C. Liu, T. Sun, P. K. Chu, Photonic spin Hall effect: A new window in D-shaped fiber by weak measurements. *Opt. Express* **27**, 14064–14074 (2019).
26. S. Chen, X. Ling, W. Shu, H. Luo, S. Wen, Precision measurement of the optical conductivity of atomically thin crystals via the photonic spin Hall effect. *Phys. Rev. Appl.* **13**, 014057 (2020).
27. B. Wang, K. Rong, E. Maguid, V. Kleiner, E. Hasman, Probing nanoscale fluctuation of ferromagnetic meta-atoms with a stochastic photonic spin Hall effect. *Nat. Nanotechnol.* **15**, 450–456 (2020).
28. S. Li, X. Li, G. Wang, S. Liu, L. Zhang, C. Zeng, L. Wang, Q. Sun, W. Zhao, W. Zhang, Multidimensional manipulation of photonic spin Hall effect with a single-layer dielectric metasurface. *Adv. Opt. Mater.* **7**, 1801365 (2018).
29. Z. Li, W. Liu, H. Cheng, S. Chen, J. Tian, Manipulation of the photonic spin Hall effect with high efficiency in gold-nanorod-based metasurfaces. *Adv. Opt. Mater.* **5**, 1700413 (2017).
30. X.-G. Luo, M.-B. Pu, X. Li, X.-L. Ma, Broadband spin Hall effect of light in single nanoapertures. *Light Sci. Appl.* **6**, e16276 (2017).
31. L. Du, Z. Xie, G. Si, A. Yang, C. Li, J. Lin, G. Li, H. Wang, X. Yuan, On-chip photonic spin Hall lens. *ACS Photonics* **6**, 1840–1847 (2019).
32. X. Ling, X. Zhou, K. Huang, Y. Liu, C.-W. Qiu, H. Luo, S. Wen, Recent advances in the spin Hall effect of light. *Rep. Prog. Phys.* **80**, 066401 (2017).
33. Y. Liu, Y. Ke, H. Luo, S. Wen, Photonic spin Hall effect in metasurfaces: A brief review. *Nanophotonics* **6**, 51–70 (2017).
34. K. Lekenta, M. Król, R. Mirek, K. Łempicka, D. Stephan, R. Mazur, P. Morawiak, P. Kula, W. Piecek, P. G. Lagoudakis, B. Piętka, J. Szczytko, Tunable optical spin Hall effect in a liquid crystal microcavity. *Light Sci. Appl.* **7**, 74 (2018).
35. A. W. Elshaari, W. Pernice, K. Srinivasan, O. Benson, V. Zwiller, Hybrid integrated quantum photonic circuits. *Nat. Photonics* **14**, 285–298 (2020).
36. F. J. García de Abajo, Optical excitations in electron microscopy. *Rev. Mod. Phys.* **82**, 209–275 (2010).
37. Q. Sun, H. Yu, K. Ueno, A. Kubo, Y. Matsuo, H. Misawa, Dissecting the few-femtosecond dephasing time of dipole and quadrupole modes in gold nanoparticles using polarized photoemission electron microscopy. *ACS Nano* **10**, 3835–3842 (2016).
38. H. Yu, Q. Sun, K. Ueno, T. Oshikiri, A. Kubo, Y. Matsuo, H. Misawa, Exploring coupled plasmonic nanostructures in the near field by photoemission electron microscopy. *ACS Nano* **10**, 10373–10381 (2016).
39. J. Langer, D. Jimenez de Aberasturi, J. Aizpurua, R. A. Alvarez-Puebla, B. Auguié, J. J. Baumberg, G. C. Bazan, S. E. J. Bell, A. Boisen, A. G. Brolo, J. Choo, D. Cialla-May, V. Deckert, L. Fabris, K. Faulds, F. Javier García de Abajo, R. Goodacre, D. Graham, A. J. Haes, C. L. Haynes, C. Huck, T. Itoh, M. Käll, J. Kneipp, N. A. Kotov, H. Kuang, E. C. Le Ru, H. K. Lee, J.-F. Li, X. Y. Ling, S. A. Maier, T. Mayerhöfer, M. Moskovits, K. Murakoshi, J.-M. Nam, S. Nie, Y. Ozaki, I. Pastoriza-Santos, J. Perez-Juste, J. Popp, A. Pucci, S. Reich, B. Ren, G. C. Schatz, T. Shegai, S. Schlücker, L.-L. Tay, K. G. Thomas, Z.-Q. Tian, R. P. Van Duyne, T. Vo-Dinh, Y. Wang, K. A. Willets, C. Xu, H. Xu, Y. Xu, Y. S. Yamamoto, B. Zhao, L. M. Liz-Marzán, Present and future of surface-enhanced raman scattering. *ACS Nano* **14**, 28–117 (2020).
40. T. Shegai, B. Brian, V. D. Miljković, M. Käll, Angular distribution of surface-enhanced Raman scattering from individual Au nanoparticle aggregates. *ACS Nano* **5**, 2036–2041 (2011).
41. A. Polman, M. Kociak, F. J. García de Abajo, Electron-beam spectroscopy for nanophotonics. *Nat. Mater.* **18**, 1158–1171 (2019).
42. D. Rossouw, M. Couillard, J. Vickery, E. Kumacheva, G. A. Botton, Multipolar plasmonic resonances in silver nanowire antennas imaged with a subnanometer electron probe. *Nano Lett.* **11**, 1499–1504 (2011).
43. T. Han, S. Zu, Z. Li, M. Jiang, X. Zhu, Z. Fang, Reveal and control of chiral cathodoluminescence at subnanoscale. *Nano Lett.* **18**, 567–572 (2018).
44. S. Zu, T. Han, M. Jiang, F. Lin, X. Zhu, Z. Fang, Deep-subwavelength resolving and manipulating of hidden chirality in achiral nanostructures. *ACS Nano* **12**, 3908–3916 (2018).
45. S. Zu, T. Han, M. Jiang, Z. Liu, Q. Jiang, F. Lin, X. Zhu, Z. Fang, Imaging of plasmonic chiral radiative local density of states with cathodoluminescence nanoscopy. *Nano Lett.* **19**, 775–780 (2019).
46. Y. Fang, R. Verre, L. Shao, P. Nordlander, M. Käll, Hot electron generation and cathodoluminescence nanoscopy of chiral split ring resonators. *Nano Lett.* **16**, 5183–5190 (2016).
47. C. I. Osorio, T. Coenen, B. J. M. Brenny, A. Polman, A. F. Koenderink, Angle-resolved cathodoluminescence imaging polarimetry. *ACS Photonics* **3**, 147–154 (2015).
48. A. V. Poshakinskiy, A. N. Poddubny, Optomechanical Kerker effect. *Phys. Rev. X* **9**, 011008 (2019).
49. T. Coenen, F. Bernal Arango, A. Femius Koenderink, A. Polman, Directional emission from a single plasmonic scatterer. *Nat. Commun.* **5**, 3250 (2014).
50. F. Bernal Arango, T. Coenen, A. F. Koenderink, Underpinning hybridization intuition for complex nanoantennas by magnetoelectric quadrupolar polarizability retrieval. *ACS Photonics* **1**, 444–453 (2014).
51. T. Coenen, A. Polman, Polarization-sensitive cathodoluminescence Fourier microscopy. *Opt. Express* **20**, 18679–18691 (2012).
52. T. Coenen, E. J. R. Vesseur, A. Polman, Angle-resolved cathodoluminescence spectroscopy. *Appl. Phys. Lett.* **99**, 143103 (2011).
53. A. B. Evlyukhin, C. Reinhardt, B. N. Chichkov, Multipole light scattering by nonspherical nanoparticles in the discrete dipole approximation. *Phys. Rev. B* **84**, 235429 (2011).
54. E. Poutrina, A. Urbas, Multipole analysis of unidirectional light scattering from plasmonic dimers. *J. Optics* **16**, 114005 (2014).
55. F. J. García de Abajo, J. Aizpurua, Numerical simulation of electron energy loss near inhomogeneous dielectrics. *Phys. Rev. B* **56**, 15873–15884 (1997).
56. G. Boudarham, M. Kociak, Modal decompositions of the local electromagnetic density of states and spatially resolved electron energy loss probability in terms of geometric modes. *Phys. Rev. B* **85**, 245447 (2012).

57. T. Wu, A. Baron, P. Lalanne, K. Vynck, Intrinsic multipolar contents of nanoresonators for tailored scattering. *Phys. Rev. A* **101**, 011803(R) (2020).
58. S. Mühlig, C. Menzel, C. Rockstuhl, F. Lederer, Multipole analysis of meta-atoms. *Metamaterials* **5**, 64–73 (2011).

Acknowledgments: We are grateful to T. Coenen from Delmic CL Solutions B.V. for help in technique support and to Z. Dang, X. He, D. Liu from Peking University for discussion about the paper. **Funding:** This work was supported by the National Key Research and Development Program of China (grant no. 2020YFA0211300), National Science Foundation of China (grant no. 12027807), Beijing Natural Science Foundation (grant no. Z180011), National Basic Research Program of China (grant nos. 2017YFA025700, 2017YFA0206000, and 2019YFA0210203), NSFC (grant nos. 61521004 and 21790364), and High-performance Computing Platform of Peking University. **Author contributions:** Z.F. supervised the project. C.C. and Q.J. conceived and designed the project. C.C. and Z.L. performed all experiments. C.C. and Q.J. accomplished all simulations. C.C. wrote the manuscript. L.Z. and M.J. provided technical supports. All authors contributed to the scientific discussions and manuscript revisions. **Competing interests:** The authors declare that they have no competing interests. **Data and materials availability:** All data needed to evaluate the conclusions in the paper are present in the paper and/or the Supplementary Materials. Additional data related to this paper may be requested from the authors.

Submitted 20 November 2020
Accepted 10 March 2021
Published 28 April 2021
10.1126/sciadv.abf8011

Citation: C. Chi, Q. Jiang, Z. Liu, L. Zheng, M. Jiang, H. Zhang, F. Lin, B. Shen, Z. Fang, Selectively steering photon spin angular momentum via electron-induced optical spin Hall effect. *Sci. Adv.* **7**, eabf8011 (2021).